Transport Anisotropy in One-dimensional Graphene Superlattice in the High Kronig-Penney Potential Limit

Tianlin Li,[1] Hanying Chen,[1] Kun Wang,[1] Yifei Hao,[1] Le Zhang,[1] Kenji Watanabe,[2] Takashi Taniguchi,[3] Xia Hong[1,*]

[1] *Department of Physics and Astronomy and Nebraska Center of Materials and Nanoscience, University of Nebraska, Lincoln, Nebraska 68588, USA*

[2] *Research Center for Electronic and Optical Materials, National Institute for Materials Science, 1-1 Namiki, Tsukuba 305-0044, Japan*

[3] *Research Center for Materials Nanoarchitectonics, National Institute for Materials Science, 1-1 Namiki, Tsukuba 305-0044, Japan*

[*] Email: xia.hong@unl.edu

Abstract

One-dimensional graphene superlattice subjected to strong Kronig-Penney (KP) potential is promising for achieving the electron-lensing effect, while previous studies utilizing the modulated dielectric gates can only yield a moderate, spatially dispersed potential profile. Here, we realize high KP potential modulation of graphene via nanoscale ferroelectric domain gating. Graphene transistors are fabricated on $PbZr_{0.2}Ti_{0.8}O_3$ back-gates patterned with periodic, 100-200 nm wide stripe domains. Due to band reconstruction, the h-BN top-gating induces satellite Dirac points in samples with current along the superlattice vector $\hat{s}$, a feature absent in samples with current perpendicular to $\hat{s}$. The satellite Dirac point position scales with the superlattice period (L) as $\propto L^{\beta}$, with β = -1.18±0.06. These results can be well explained by the high KP potential scenario, with the Fermi velocity perpendicular to $\hat{s}$ quenched to about 1% of that for pristine graphene. Our study presents a promising material platform for realizing electron supercollimation and investigating flat band phenomena.

Two-dimensional (2D) van der Waals materials subjected to artificially designed superlattice (SL) potential modulation are versatile platforms exhibiting a rich variety of emergent phenomena [1-3], including band reconstruction and Brillouin zone folding [4-12], correlation driven Mott transitions [13], superconductivity [14], magnetism [15, 16], ferroelectricity [17, 18], and topological orders [19]. Among them, the one-dimensional (1D) graphene superlattice (GSL) has gained considerable research interests [1] as the strong anisotropy and flattening of energy bands [6, 7, 20] can lead to electron-supercollimation effect [21, 22] as well as correlated states. While 1D GSL has been intensively investigated theoretically [1, 6, 20-26], only few experimental demonstrations have been reported, exploiting a dielectric gate with either nanoscale electrode-arrays [7] or periodic thickness-modulation to generate the Kronig-Penney (KP) potential [11]. The modulated-dielectric-gating approach has two intrinsic limitations. First, the doping capacity of conventional dielectrics such as Al_2O_3 and SiO_2 is typically $<10^{13}$ cm^{-2}, which imposes only moderate KP potential in the graphene channel. The resulting electronic structure, even though distorted from the isotropic configuration, is not viable for hosting the electron-lensing effect. Second, due to the finite gate-thickness, the locally applied gate-bias becomes spatially dispersed when mapped on the conducting channel [Fig. 1(a)]. To date, 1D GSL modulation in the high KP-potential limit has never been achieved experimentally.

A promising material scheme to overcome these challenges is to exploit a ferroelectric gate with periodically patterned domain structures [27], utilizing the nonvolatile, switchable polarization to induce the SL potential modulation in graphene. The ferroelectric field effect has previously been adopted to induce nonvolatile modulation of the resistance and quantum transport in graphene [28-30]. Combining it with nanoscale domain patterning further enables the design of reconfigurable functionalities [31-35] and directional conduction paths [36] in a 2D channel. For ferroelectrics such as oxide $Pb(Zr,Ti)O_3$ [37] and copolymer P(VDF-TrFE) [36], the remnant polarization corresponds to a high 2D carrier density well exceeding 10^{13} cm^{-2}. Since the surface bound-charge of ferroelectric domains is in direct contact with the 2D channel, the induced density variation in graphene across a sharp domain wall (DW) can produce a step-like potential change [Fig. 1(a)].

In this work, we report the first realization of 1D GSL in the high KP-potential limit via nanoscale domain patterning in a ferroelectric $PbZr_{0.2}Ti_{0.8}O_3$ (PZT) gate [Fig. 1(b)]. Monolayer graphene field effect transistors (FETs) are fabricated on prepatterned periodic stripe domains of

PZT, with the period L varying from 200 to 300 nm. The polarization reversal of PZT shifts the Fermi level (E_F) of graphene by up to 0.9 eV. For the GSL samples, satellite Dirac points (DPs) emerge in the longitudinal resistance along the SL vector $\hat{s}$ and evolve into multiple Landau-fan branches in high magnetic fields, a feature absent for resistance perpendicular to $\hat{s}$. The average carrier density interval between consecutive DPs scales with the SL period as $\propto L^{\beta}$, with $\beta = -1.18 \pm 0.06$, which can be well described by the band structure of 1D GSL under high KP potential. The Fermi velocity perpendicular to $\hat{s}$ is quenched to about 1% of that for pristine graphene, paving the path for designing the electron-lensing effect.

We work with 50 nm epitaxial (001) PZT films deposited on 10 nm $La_{0.67}Sr_{0.33}MnO_3$ (LSMO) buffered $SrTiO_3$ (STO) substrates, with the polar axis of PZT along surface normal. The PZT films have high crystallinity and surface roughness of 4-5 Å, with details in the Supplemental Material [38]. Piezoresponse force microscopy (PFM) switching hysteresis shows robust ferroelectric switching with coercive voltages of +1.2/-2.5 V for the polarization down (P_{down}) and up (P_{up}) states [Fig. 1(c)]. In the ambient condition, the surface bound charges of PZT would be quickly screened by charged adsorbates or trap states prior to graphene transfer and thus do not induce doping in graphene at 300 K [27, 37]. Upon cooling, the polarization field increases due to the pyroelectric effect [29], and we leverage the additional polarization to dope graphene at low temperature. We characterize the PZT pyroelectric effect-induced variation of carrier density in graphene using a Hall bar device [38]. Figure 1(d) shows the temperature dependence of the converted polarization with respect to the 300 K value, $\Delta P = |P\text{-}P(300\ \text{K})|$, which yields a polarization increase of about ~2.5 μC cm^{-2} at 2 K. Switching PZT polarization ($2\Delta P$) can thus lead to a 2D carrier density of up to 3×10^{13} cm^{-2} in graphene.

To fabricate the 1D GSL, we prepattern Cr/Au (2 nm/10 nm) electrodes on PZT in the four-point configuration. Periodic stripe domains are written between the voltage probes by conductive atomic force microscopy in two orientations, either parallel or perpendicular to the current path. The width of the P_{down} (P_{up}) domains is 100 nm (100-200 nm), yielding a SL period of L = 200-300 nm [Fig. 1(e)] [38]. Monolayer graphene flakes with h-BN top-layers (25-40 nm) are transferred on PZT using the dry transfer approach [39], in direct contact with the prepatterned domain structures and Au electrodes [Fig. 1(f)]. Cr/Au (10 nm/50 nm) are then deposited on h-BN as the global top-gate electrode [Fig. 1(g)]. Magnetotransport measurements are performed in

a Quantum Design Physical Property Measurement System using the standard lock-in technique with 50 nA current. The results reported are based on six GSL samples with current along the SL vector $\hat{s}$ (denoted as D1-D6) and one GSL sample with current perpendicular to $\hat{s}$ (denoted as D7), as summarized in Supplemental Table 1 [38]. PFM studies show that the domain structure is robust against sample fabrication and electrical measurements [38].

Figure 2 shows the sheet resistance $R_{\square}$ as a function of electron doping δn induced by the top-gate at 2 K for two GSL samples, D1 with L = 205±6 nm [Fig. 2(a)] and D7 with L = 199±6 nm [Fig. 2(b)]. As $\hat{s}$ is along x-axis in the laboratory coordinates, we denote $R_{\square}$ for these two samples as R_{xx} and R_{yy}, respectively. Here $\delta n = \alpha V_g$, where V_g is the top-gate voltage and $\alpha = \varepsilon_r\varepsilon_0/ed$ is the gating efficiency, with $\varepsilon_r = 3.76$ the dielectric constant of h-BN [40], ε_0 the vacuum permittivity, e the elementary charge, and d the h-BN thickness [38]. For comparison, we also show $R_{\square}(\delta n)$ for a pristine graphene sample [Fig. 2(a)]. The pristine sample exhibits a single peak at the charge neutral point (CNP), with the field effect mobility μ_{FE} of about 20,000 $cm^2V^{-1}s^{-1}$ for holes and 12,000 $cm^2V^{-1}s^{-1}$ for electrons. For the doping level of interest in this study ($|n|$ = 2-8×10^{12} cm^{-2}), this corresponds to a mean free path of about 200-660 nm, confirming that the SL induced band reconstruction is viable at the chosen SL period (200-300 nm). For sample D1, $R_{xx}(\delta n)$ shows two more satellite peaks symmetrically displaced from the main Dirac point, locating at δn = -1.34×10^{12} cm^{-2} and 1.73×10^{12} cm^{-2} [Fig. 2(a)]. This carrier density level is more than one order of magnitude smaller than that expected for pyroelectric polarization doping, excluding inhomogeneous doping as the origin of the emergent peaks. For sample D7, $R_{yy}(\delta n)$ exhibits a single peak [Fig. 2(b)], similar to that of the pristine graphene.

The transport anisotropy between R_{xx} and R_{yy} is a direct manifestation of the emergent 1D GSL [6, 7, 11] induced by the periodic ferroelectric polarization gating effect. At 2 K, the pyroelectric effect induced ΔP generates a KP-type potential with an equivalent amplitude of about $V_0 = 2\hbar v_F\sqrt{\pi\Delta P(2\text{ K})/e} = 0.9$ eV [Fig. 1(a)], where $v_F = 10^8$ cm s^{-1} is the Fermi velocity of graphene. This results in a renormalized band structure, with the Fermi velocity unchanged along $\hat{s}$ (v_x) and highly suppressed perpendicular to $\hat{s}$ (v_y) [22]. The extra peaks observed in $R_{xx}(\delta n)$ correspond to the emergent DPs at the band crossing of the highly folded Brillouin zone [1, 6]. The positions of the satellite DPs do not vary significantly from 1.8 to 10 K (Supplemental Fig. S7) [38], consistent with the saturation of ΔP in PZT below 100 K [Fig. 1(d)]. In contrast, $R_{yy}(\delta n)$

only exhibits a single resistance peak at the original CNP due to the suppressed Klein tunneling along the stripe domains [6, 23, 41, 42]. The broadening of the peak compared with pristine graphene can be attributed to either the suppression of relaxation time associated with the high density of states of the SL or the nanoscale variation of current orientation with respect to *y*-direction. Similar broadening has been reported previously in GSL fabricated via modulated dielectric gates with increasing KP potential [11].

We then investigate the transport anisotropy of GSL in magnetic fields [7, 11]. Figure 3(a) shows R_{xx} versus δn and magnetic field B for sample D1, where we observe Shubnikov de Haas oscillations associated with three sets of Landau-fan structures [38]. The central Landau-fan branches out from the original DP, while the two satellite fans emanate from δn = -1.41×10^{12} cm^{-2} and 2.16×10^{12} cm^{-2}, consistent with the emergent DPs at zero field [Fig. 2(a)]. In Fig. 3(b), we model the Landau-fan structures using $n = \nu eB/h + n_{\mathrm{DP}}$, with $\nu = 4l + 2$ the filling factors, l the Landau-level index, h the Plank constant, and n_{DP} the carrier density of the associated DP position. As shown in Fig. 3(a), the simulated Landau fans are in excellent agreement with the experimental R_{xx} data. Figure 3(c) shows the R_{yy} data of sample D7, which possesses a similar SL period. As expected, it exhibits only one set of Landau fan emanating from the original DP [Fig. 3(c)-(d)]. Furthermore, at high magnetic fields, R_{xx} is more than one order of magnitude higher than R_{yy}, similar as that reported in GSLs with modulated dielectric gates, which has been attributed to the highly localized electron wavefunction along $\hat{s}$ in magnetic fields [11].

The emergent satellite DPs are observed in R_{xx} taken on all six GSL samples with current along $\hat{s}$ (Supplemental Fig. S9) [38]. We adopt multiple-peak fits to $R_{xx}(\delta n)$ to identify the order of extra DPs [38]. To minimize the error in calculating the average carrier density interval between two consecutive DPs Δn_{DP}, we select two most prominent peaks at high doping levels, with one from the hole branch (order N_h at $n_{\mathrm{DP,h}}$) and one from the electron branch (order N_e at $n_{\mathrm{DP,e}}$), and deduce $\Delta n_{\mathrm{DP}} = (n_{\mathrm{DP,e}} - n_{\mathrm{DP,h}})/(N_e - N_h)$. Figure 4 shows Δn_{DP} as a function of L, which can be well described by:

$$\Delta n_{\mathrm{DP}} = AL^{\beta}, \quad \text{with } \beta = -1.18 \pm 0.06. \tag{1}$$

Here A is the proportionality constant. To understand the L-dependence of Δn_{DP}, we model the band structures of 1D GSL at moderate and high KP potentials. For 1D GSL under the long wavelength approximation, the Hamiltonian can be written as $H = v_F \vec{\boldsymbol{\sigma}} \cdot \hat{\boldsymbol{p}} + V_{1\mathrm{D}}(x)$, with $\vec{\boldsymbol{\sigma}}$ the

Pauli matrices vector, $\hat{\boldsymbol{p}}$ the momentum operator, and $V_{1\mathrm{D}}(x)$ the 1D scalar KP potential [1, 6, 24]. Assuming the widths of the well and barrier regions are W_w and W_b, respectively [Fig. 1(a)], we deduce the dispersion relation $E(k_x, k_y)$ using the transfer matrix method [6]:

$$\cos(k_x L) = \cos\left(\lambda_w \frac{W_w}{L}\right)\cos\left(\lambda_b \frac{W_b}{L}\right) - G\sin\left(\lambda_w \frac{W_w}{L}\right)\sin\left(\lambda_b \frac{W_b}{L}\right), \quad (2)$$

with $\lambda_{w,b} = \left(\epsilon_{w,b}^2 - k_y^2 L^2\right)^{\frac{1}{2}}$, $G = \frac{\epsilon_w \epsilon_b - k_y^2 L^2}{\lambda_w \lambda_b}$, $\epsilon_w = \epsilon + u\frac{W_w}{L}$, and $\epsilon_b = \epsilon - u\frac{W_b}{L}$. Here $\epsilon_{w,b}$ can be viewed as the dimensionless effective energy of the wavefunction in the well or barrier region, which is given by the dimensionless dispersion $\epsilon = \frac{EL}{\hbar v_F}$ modified by the scaled dimensionless KP potential $u = \frac{V_0 L}{\hbar v_F}$.

We first consider the case for the moderate KP potential as those generated by the modulated dielectric gates [7, 11]. Figure 5(a) shows the modeled band structures for $u = 9\pi$, where new bands emerge along $\hat{s}$ with periodic band crossing points locating at $k_x = N\pi/L$ for the Nth reconstructed band. The isopotential contours show very complicated features, hosting multiple satellite DPs in one band [Fig. 5(b)]. The Fermi velocity becomes anisotropic, with v_x remaining unchanged and v_y suppressed to about $0.1v_F$ at the original DP. With increasing u, v_y is oscillatory with a damped envelop following $v_y = v_F\sin(u/4)/(u/4)$ [6]. For our 1D GSL generated by ferroelectric domains, the SL period L = 200 nm corresponds to a high $u \sim 90\pi$, which quenches v_y to about 0.01 v_F. As shown in Fig. 5(c), the SL energy band possesses a highly flattened energy dispersion that can be approximated as $E = \pm\hbar v_F(k_x + 2N\pi/L)$.

We then evaluate the relation between E_F and n for the SL band structure at the high u limit. From Luttinger theorem, the carrier density is given by the surface area of the Fermi surface. As shown in Fig. 5(d), the isopotential contours at $u = 90\pi$ closely resemble rectangles that extend to the entire Brillouin zone. The enclosed area of each isopotential contour can thus be approximated as αk_x, with α on the order of the size of graphene Brillouin zone. Given that $n = \alpha k_x/\pi^2$, we obtain $E_F = \hbar v_F n\pi^2/\alpha$. For the satellite DPs located at the Nth band crossing, $E = \hbar v_F \frac{N\pi}{L}$ and the corresponding doping level is $\Delta n_{\mathrm{DP}} = N\alpha/\pi L \propto 1/L$. The inversely proportional relation between Δn_{DP} and L closely resembles our experimental results (Fig. 4 and Eq. 1). In sharp contrast, in a moderate KP potential, the extra DP position exhibits an opposite trend and increases

with the SL period L at a given KP potential V_0 [11]. Setting the fitted proportionality constant in Eq. 1 as $A = \alpha/\pi$, we obtain $\alpha = 26.2\ \mathrm{nm}^{-1}$, which is in excellent agreement with the Brillouin zone size of graphene $2\pi/a_0 = 25.5\ \mathrm{nm}^{-1}$, further confirming that our 1D GSL samples are in the high KP potential limit.

The extremely flattened SL band associated with the high KP potential, on the other hand, can also limit the observation of extra DPs, as the enhanced density of states broadens the resistance peaks [11]. Compared with the multi-satellite DPs observed in 1D GSL subjected to moderate KP potential, *e.g.*, those generated by modulated dielectric gate [7, 11], our samples only exhibit a couple of extra peaks in $R_{xx}(V_g)$, which reflects the flattened dispersion at the band crossings [Fig. 5(c)]. There are additional factors that can compromise the observation of the emergent DPs. First, the ferroelectric DWs are intrinsically rough [43], which leads to a randomness in the SL period L and perturbs the SL band reconstruction [44]. It has been shown theoretically that the transport signature of extra DPs can be damped by ~90% at 5% randomness in the high KP potential limit [45]. Second, the DW roughness for PZT on LSMO is about 6 nm [38]. To minimize its impact, we work with SL period $L \geq 200$ nm. Even though the typical mean free path of our 1D GSL samples is larger than L, these two length scales become comparable at lower carrier density, which may blur the ideal SL band structure and lead to decoherent transport. Third, we work with finite numbers of the stripe domains (35-50) [38], and the convoluted effect of finite SL modulation also broadens the reconstructed band. It is worth noting that the limitations associated with a PZT back-gate, including the compromised KP potential due to interfacial screening charges and the non-programmable domain structure after sample fabrication, can be overcome by adopting a suspended PZT membrane top-gate [34, 35].

In conclusion, we realize 1D GSL via periodic ferroelectric stripe domains patterned in a PZT back-gate. The samples exhibit high transport anisotropy between the current directions along and perpendicular to the SL vector, with satellite DPs emerging in the former configuration due to Brillouin zone folding. The scaling behavior of the carrier density interval between consecutive DPs with the SL period can be well modeled by the reconstructed band structure subject to high KP potential. The ferroelectric-domain-controlled 1D GSL presents a promising material platform for studying electron supercollimation as well as designing collective phenomena associated with flat bands, including magnetism, superconductivity, and topological sub-bands.

Acknowledgement

The authors thank Wuzhang Fang, Dawei Li, Qiuchen Wu, and Yuhan Zhang for the valuable discussions, and Anandakumar Sarella for technical assistance. This work was supported by the U.S. Department of Energy (DOE), Office of Science, Basic Energy Sciences (BES), under Award No. DE-SC0016153, NSF EPSCoR RII Track-1: Emergent Quantum Materials and Technologies (EQUATE), under Award No. OIA-2044049, and Nebraska Center for Energy Sciences Research (NCESR). K.W. and T.T. acknowledge support from the JSPS KAKENHI (Grant Numbers 20H00354, 21H05233 and 23H02052) and World Premier International Research Center Initiative (WPI), MEXT, Japan. The research was performed, in part, in the Nebraska Nanoscale Facility: National Nanotechnology Coordinated Infrastructure, the Nebraska Center for Materials and Nanoscience, which are supported by NSF ECCS: 2025298, and the Nebraska Research Initiative.

References

[1] M. Barbier, P. Vasilopoulos, and F. M. Peeters, Single-layer and bilayer graphene superlattices: collimation, additional Dirac points and Dirac lines, Philosophical Transactions of the Royal Society A: Mathematical, Physical and Engineering Sciences **368**, 5499 (2010).

[2] Y. K. Ryu, R. Frisenda, and A. Castellanos-Gomez, Superlattices based on van der Waals 2D materials, Chemical Communications **55**, 11498 (2019).

[3] F. He, Y. Zhou, Z. Ye, S.-H. Cho, J. Jeong, X. Meng, and Y. Wang, Moiré Patterns in 2D Materials: A Review, ACS Nano **15**, 5944 (2021).

[4] C.-H. Park, Y.-W. Son, L. Yang, M. L. Cohen, and S. G. Louie, Landau Levels and Quantum Hall Effect in Graphene Superlattices, Physical Review Letters **103**, 046808 (2009).

[5] L. Brey, and H. A. Fertig, Emerging Zero Modes for Graphene in a Periodic Potential, Physical Review Letters **103**, 046809 (2009).

[6] M. Barbier, P. Vasilopoulos, and F. M. Peeters, Extra Dirac points in the energy spectrum for superlattices on single-layer graphene, Physical Review B **81**, 075438 (2010).

[7] S. Dubey, V. Singh, A. K. Bhat, P. Parikh, S. Grover, R. Sensarma, V. Tripathi, K. Sengupta, and M. M. Deshmukh, Tunable Superlattice in Graphene To Control the Number of Dirac Points, Nano Letters **13**, 3990 (2013).

[8] C. R. Dean, L. Wang, P. Maher, C. Forsythe, F. Ghahari, Y. Gao, J. Katoch, M. Ishigami, P. Moon, M. Koshino, T. Taniguchi, K. Watanabe, K. L. Shepard, J. Hone, and P. Kim, Hofstadter's butterfly and the fractal quantum Hall effect in moiré superlattices, Nature **497**, 598 (2013).

[9] B. Hunt, J. D. Sanchez-Yamagishi, A. F. Young, M. Yankowitz, B. J. LeRoy, K. Watanabe, T. Taniguchi, P. Moon, M. Koshino, P. Jarillo-Herrero, and R. C. Ashoori, Massive Dirac Fermions and Hofstadter Butterfly in a van der Waals Heterostructure, Science **340**, 1427 (2013).

[10] L. A. Ponomarenko, R. V. Gorbachev, G. L. Yu, D. C. Elias, R. Jalil, A. A. Patel, A. Mishchenko, A. S. Mayorov, C. R. Woods, J. R. Wallbank, M. Mucha-Kruczynski, B. A. Piot, M. Potemski, I. V. Grigorieva, K. S. Novoselov, F. Guinea, V. I. Fal'ko, and A. K. Geim, Cloning of Dirac fermions in graphene superlattices, Nature **497**, 594 (2013).

[11] Y. Li, S. Dietrich, C. Forsythe, T. Taniguchi, K. Watanabe, P. Moon, and C. R. Dean, Anisotropic band flattening in graphene with one-dimensional superlattices, Nature Nanotechnology **16**, 525 (2021).

[12] C. Forsythe, X. Zhou, K. Watanabe, T. Taniguchi, A. Pasupathy, P. Moon, M. Koshino, P. Kim, and C. R. Dean, Band structure engineering of 2D materials using patterned dielectric superlattices, Nature Nanotechnology **13**, 566 (2018).

[13] Y. Cao, V. Fatemi, A. Demir, S. Fang, S. L. Tomarken, J. Y. Luo, J. D. Sanchez-Yamagishi, K. Watanabe, T. Taniguchi, E. Kaxiras, R. C. Ashoori, and P. Jarillo-Herrero, Correlated insulator behaviour at half-filling in magic-angle graphene superlattices, Nature **556**, 80 (2018).

[14] Y. Cao, V. Fatemi, S. Fang, K. Watanabe, T. Taniguchi, E. Kaxiras, and P. Jarillo-Herrero, Unconventional superconductivity in magic-angle graphene superlattices, Nature **556**, 43 (2018).

[15] A. L. Sharpe, E. J. Fox, A. W. Barnard, J. Finney, K. Watanabe, T. Taniguchi, M. A. Kastner, and D. Goldhaber-Gordon, Emergent ferromagnetism near three-quarters filling in twisted bilayer graphene, Science **365**, 605 (2019).

[16] E. Anderson, F.-R. Fan, J. Cai, W. Holtzmann, T. Taniguchi, K. Watanabe, D. Xiao, W. Yao, and X. Xu, Programming correlated magnetic states with gate-controlled moiré geometry, Science **381**, 325 (2023).

[17] K. Yasuda, X. Wang, K. Watanabe, T. Taniguchi, and P. Jarillo-Herrero, Stacking-engineered ferroelectricity in bilayer boron nitride, Science **372**, 1458 (2021).

[18] D. R. Klein, L.-Q. Xia, D. MacNeill, K. Watanabe, T. Taniguchi, and P. Jarillo-Herrero, Electrical switching of a bistable moiré superconductor, Nature Nanotechnology **18**, 331 (2023).

[19] M. Serlin, C. L. Tschirhart, H. Polshyn, Y. Zhang, J. Zhu, K. Watanabe, T. Taniguchi, L. Balents, and A. F. Young, Intrinsic quantized anomalous Hall effect in a moiré heterostructure, Science **367**, 900 (2020).

[20] C.-H. Park, L. Yang, Y.-W. Son, M. L. Cohen, and S. G. Louie, Anisotropic behaviours of massless Dirac fermions in graphene under periodic potentials, Nature Physics **4**, 213 (2008).

[21] S. Choi, C.-H. Park, and S. G. Louie, Electron Supercollimation in Graphene and Dirac Fermion Materials Using One-Dimensional Disorder Potentials, Physical Review Letters **113**, 026802 (2014).

[22] C.-H. Park, Y.-W. Son, L. Yang, M. L. Cohen, and S. G. Louie, Electron Beam Supercollimation in Graphene Superlattices, Nano Letters **8**, 2920 (2008).

[23] C. Bai, and X. Zhang, Klein paradox and resonant tunneling in a graphene superlattice, Physical Review B **76**, 075430 (2007).

[24] M. Barbier, P. Vasilopoulos, and F. M. Peeters, Dirac electrons in a Kronig-Penney potential: Dispersion relation and transmission periodic in the strength of the barriers, Physical Review B **80**, 205415 (2009).

[25] C.-H. Park, L. Yang, Y.-W. Son, M. L. Cohen, and S. G. Louie, New Generation of Massless Dirac Fermions in Graphene under External Periodic Potentials, Physical Review Letters **101**, 126804 (2008).

[26] A. De Martino, L. Dell'Anna, L. Handt, A. Miserocchi, and R. Egger, Two-dimensional Dirac fermions in a mass superlattice, Physical Review B **107**, 115420 (2023).

[27] X. Hong, Emerging ferroelectric transistors with nanoscale channel materials: the possibilities, the limitations, Journal of Physics: Condensed Matter **28**, 103003 (2016).

[28] Y. Zheng, G.-X. Ni, C.-T. Toh, M.-G. Zeng, S.-T. Chen, K. Yao, and B. Özyilmaz, Gate-controlled nonvolatile graphene-ferroelectric memory, Applied Physics Letters **94**, 163505 (2009).

[29] A. Rajapitamahuni, J. Hoffman, C. H. Ahn, and X. Hong, Examining Graphene Field Effect Sensors for Ferroelectric Thin Film Studies, Nano Letters **13**, 4374 (2013).

[30] H. Chen, T. Li, Y. Hao, A. Rajapitamahuni, Z. Xiao, S. Schoeche, M. Schubert, and X. Hong, Remote surface optical phonon scattering in ferroelectric $Ba_{0.6}Sr_{0.4}TiO_3$ gated graphene, Journal of Applied Physics **132**, 154301 (2022).

[31] Z. Xiao, J. Song, D. K. Ferry, S. Ducharme, and X. Hong, Ferroelectric-Domain-Patterning-Controlled Schottky Junction State in Monolayer MoS_2, Physical Review Letters **118**, 236801 (2017).

[32] A. Lipatov, T. Li, N. S. Vorobeva, A. Sinitskii, and A. Gruverman, Nanodomain Engineering for Programmable Ferroelectric Devices, Nano Letters **19**, 3194 (2019).

[33] G. Wu, B. Tian, L. Liu, W. Lv, S. Wu, X. Wang, Y. Chen, J. Li, Z. Wang, S. Wu, H. Shen, T. Lin, P. Zhou, Q. Liu, C. Duan, S. Zhang, X. Meng, S. Wu, W. Hu, X. Wang, J. Chu, and J. Wang, Programmable transition metal dichalcogenide homojunctions controlled by nonvolatile ferroelectric domains, Nature Electronics **3**, 43 (2020).

[34] D. Li, X. Huang, Q. Wu, L. Zhang, Y. Lu, and X. Hong, Ferroelectric Domain Control of Nonlinear Light Polarization in MoS_2 via $PbZr_{0.2}Ti_{0.8}O_3$ Thin Films and Free-Standing Membranes, Advanced Materials **35**, 2208825 (2023).

[35] Q. Wu, K. Wang, A. Simpson, Y. Hao, J. Wang, D. Li, and X. Hong, Electrode Effect on Ferroelectricity in Free-Standing Membranes of $PbZr_{0.2}Ti_{0.8}O_3$, ACS Nanoscience Au (2023).

[36] D. Li, S. Sun, Z. Xiao, J. Song, D.-F. Shao, E. Y. Tsymbal, S. Ducharme, and X. Hong, Giant Transport Anisotropy in ReS_2 Revealed via Nanoscale Conducting-Path Control, Physical Review Letters **127**, 136803 (2021).

[37] C. Baeumer, S. P. Rogers, R. Xu, L. W. Martin, and M. Shim, Tunable Carrier Type and Density in Graphene/$PbZr_{0.2}Ti_{0.8}O_3$ Hybrid Structures through Ferroelectric Switching, Nano Letters **13**, 1693 (2013).

[38] See Supplemental Material at xxx for details on the sample fabrication and characterization, magnetotransport results, and data analysis.

[39] K. Kinoshita, R. Moriya, M. Onodera, Y. Wakafuji, S. Masubuchi, K. Watanabe, T. Taniguchi, and T. Machida, Dry release transfer of graphene and few-layer h-BN by utilizing thermoplasticity of polypropylene carbonate, npj 2D Materials and Applications **3**, 22 (2019).

[40] A. Laturia, M. L. Van de Put, and W. G. Vandenberghe, Dielectric properties of hexagonal boron nitride and transition metal dichalcogenides: from monolayer to bulk, npj 2D Materials and Applications **2**, 6 (2018).

[41] A. F. Young, and P. Kim, Electronic Transport in Graphene Heterostructures, Annual Review of Condensed Matter Physics **2**, 101 (2011).

[42] S. Chen, Z. Han, M. M. Elahi, K. M. M. Habib, L. Wang, B. Wen, Y. Gao, T. Taniguchi, K. Watanabe, J. Hone, A. W. Ghosh, and C. R. Dean, Electron optics with p-n junctions in ballistic graphene, Science **353**, 1522 (2016).

[43] K. Wang, Y. Hao, L. Zhang, Y. Zhang, X. Chen, and X. Hong, Effect of correlated oxide electrodes on disorder pinning and thermal roughening of ferroelectric domain walls in epitaxial $PbZr_{0.2}Ti_{0.8}O_3$ thin films, Physical Review Materials **5**, 074402 (2021).

[44] Y. P. Bliokh, V. Freilikher, S. Savel'ev, and F. Nori, Transport and localization in periodic and disordered graphene superlattices, Physical Review B **79**, 075123 (2009).

[45] N. Abedpour, A. Esmailpour, R. Asgari, and M. R. R. Tabar, Conductance of a disordered graphene superlattice, Physical Review B **79**, 165412 (2009).

Figure Captions

FIG. 1. (a) Schematics of 1D GSLs imposed via modulated dielectric (DE) gate (top) and ferroelectric (FE) domain structure (bottom), and the corresponding potential profiles $V(x)$. (b) Sample schematic. (c) PFM amplitude (top) and phase (bottom) switching hysteresis of 50 nm PZT/10 nm LSMO on STO. (d) $\Delta P(T)$ for PZT. (e) PFM phase image of stripe domains with period of L = 205 nm on PZT. (f) Optical image of a h-BN/graphene stack transferred on prepatterned domain structure of PZT. The dashed (dotted) lines highlight the graphene edges (SL region). (g) Optical image of the same sample after the deposition of Au top-gate electrode.

FIG. 2. (a) $R_{\square}(\delta n)$ for pristine graphene and sample D1. (b) $R_{\square}(\delta n)$ for sample D7. Upper panels: schematics of GSL configurations.

FIG. 3. (a) R_{xx} *vs.* δn and B for sample D1. The dashed lines illustrate the modeled Landau fans emanating from the original and satellite DPs. (b) Modeled Landau fans in (a) with the filling factors labeled. (c) R_{yy} *vs.* δn and B for sample D7. The dashed lines illustrate the modeled Landau fan emanating from the original DP. (d) Modeled Landau fan in (c) with the filling factors labeled. Resistance in (a) and (c) is on the log scale.

FIG. 4. Δn_{DP} *vs.* L for samples D1-D6 with a fit to Eq. 1 (dashed line) on linear and (inset) semi-log scales. The error bars for Δn_{DP} and L are deduced from the variation in h-BN thickness (Supplemental Table S1) and DW roughness, respectively [38].

FIG. 5. (a) Calculated band structure at $u = 9\pi$ and $W_w = W_b$, and (b) its dimensionless energy contour plot of conduction band. (c) Calculated band structure at $u = 90\pi$ and $W_w = W_b$, and (d) its dimensionless energy contour plot of conduction band. The dimensionless energy values are labeled in (b) and (d).

Figure 1

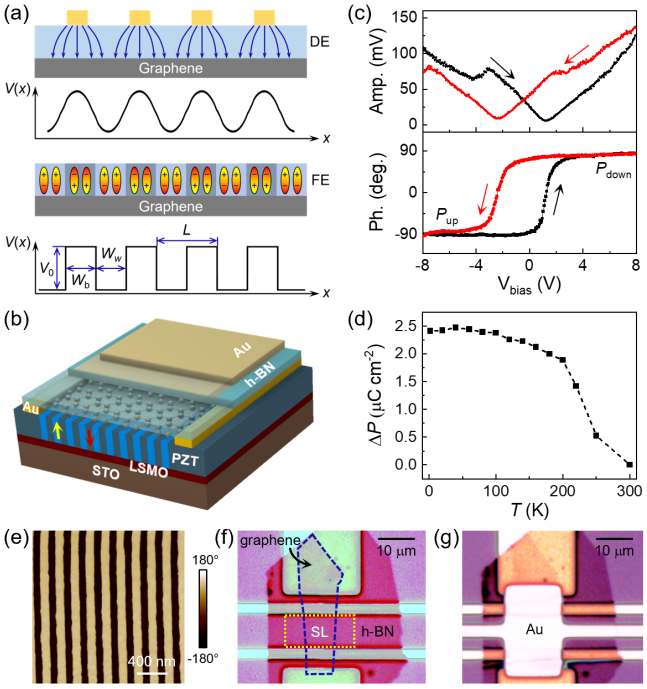
(a)
DE
Graphene
V(x)
x
FE
Graphene
L
V(x)
V_0
W_w
W_b
x
(b)
Au
h-BN
Au
PZT
STO
LSMO
(c)
Amp. (mV)
150
100
50
0
Ph. (deg.)
90
0
-90
P_{down}
P_{up}
-8
-4
0
4
8
V_{bias} (V)
(d)
ΔP (μC cm^{-2})
2.5
2.0
1.5
1.0
0.5
0.0
0
100
200
300
T (K)
(e)
180°
-180°
400 nm
(f)
graphene
10 μm
SL
h-BN
(g)
10 μm
Au

Figure 2

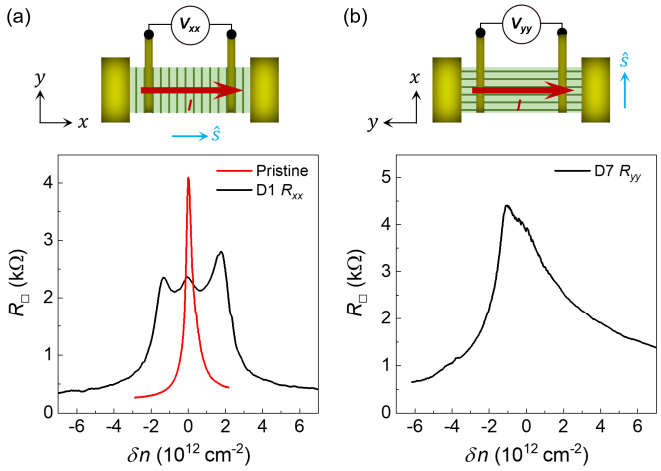
(a)
V_{xx}
y
x
I
$\hat{s}$
Pristine
D1 R_{xx}
$R_\square$ (kΩ)
δn (10^{12} cm^{-2})
(b)
V_{yy}
x
y
I
$\hat{s}$
D7 R_{yy}
$R_\square$ (kΩ)
δn (10^{12} cm^{-2})

Figure 3

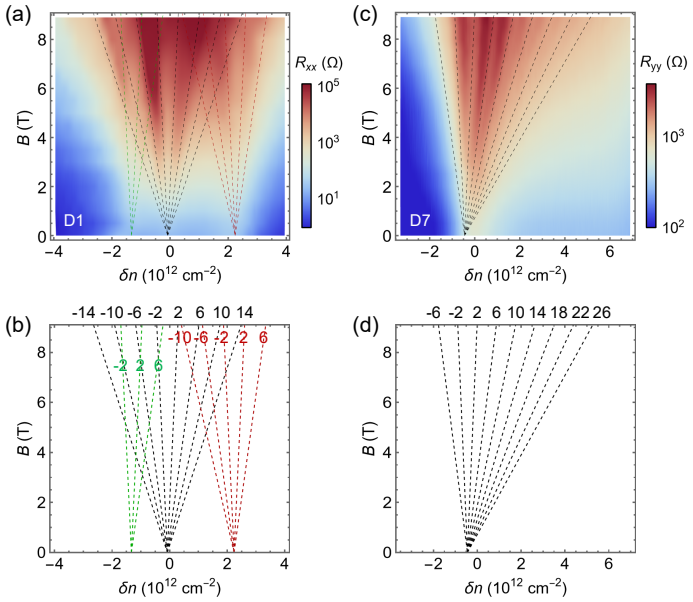
(a)
(b)
(c)
(d)
D1
D7
B (T)
δn (10^12 cm^−2)
R_xx (Ω)
R_yy (Ω)
10^5
10^3
10^1
10^2
-14 -10 -6 -2 2 6 10 14
-10 -6 -2 2 6
-2 2 6
-6 -2 2 6 10 14 18 22 26

Figure 4

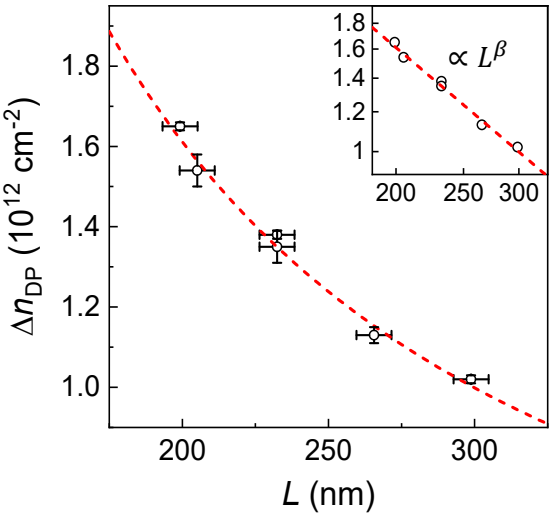

Figure 5